

# **EFFECTS OF FLAME TEMPERATURE RATIO ON BLUFF BODY WAKES**

A Thesis  
Presented to  
The Academic Faculty

by

Julia Lundrigan

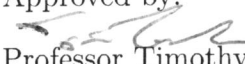
In Partial Fulfillment  
of the Requirements for the Degree  
Bachelor of Science in the  
School of Aerospace Engineering

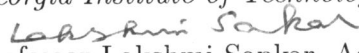
Georgia Institute of Technology  
May 2012

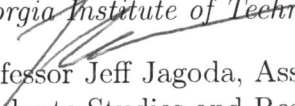
Copyright © 2012 by Julia Lundrigan

# EFFECTS OF FLAME TEMPERATURE RATIO ON BLUFF BODY WAKES

Approved by:

  
Professor Timothy Lieuwen, Advisor  
School of Aerospace Engineering  
*Georgia Institute of Technology*

  
Professor Lakshmi Sankar, Associate Chair  
for Undergraduate Programs  
School of Aerospace Engineering  
*Georgia Institute of Technology*

  
Professor Jeff Jagoda, Associate Chair for  
Graduate Studies and Research  
School of Aerospace Engineering  
*Georgia Institute of Technology*

Date Approved: 04 May 2012

## ACKNOWLEDGEMENTS

I want to acknowledge and thank those who assisted and mentored me through the six semesters of my undergraduate research in the Combustion Lab at Georgia Tech, particularly Dr. Tim Lieuwen, Ben Emerson, and Bobby Noble. I also want to thank the Undergraduate Research Opportunities office at Georgia Tech for their financial support in the form of PURA for my research.

# TABLE OF CONTENTS

<b>ACKNOWLEDGEMENTS</b>	<b>iii</b>
<b>LIST OF TABLES</b>	<b>vi</b>
<b>LIST OF FIGURES</b>	<b>vii</b>
<b>LIST OF SYMBOLS OR ABBREVIATIONS</b>	<b>ix</b>
<b>SUMMARY</b>	<b>xi</b>
<b>I INTRODUCTION</b>	<b>1</b>
1.1 Combustion Instabilities	2
1.1.1 Acoustic/Flame Coupling	3
1.1.2 Flame-Vortex Interactions	4
1.2 Bluff Body Flows	5
1.2.1 Hydrodynamic Instabilities	6
1.2.2 Absolute and Convective Instabilities	7
1.3 Reacting Flows	9
1.3.1 Wake Structure	10
1.3.2 Flame Stabilization	10
1.4 Summary	11
<b>II MATERIALS AND METHODS</b>	<b>15</b>
2.1 Experimental Facility	15
2.2 Test Conditions	17
2.3 Diagnostic Equipment	18
2.4 Bluff Body Variation	20
2.5 Data Analysis	21
2.5.1 High Speed Video	21
2.5.2 PIV	22

<b>III RESULTS AND DISCUSSION . . . . .</b>	<b>23</b>
3.1 Spectral and Correlation Analysis . . . . .	23
3.2 Intermittency . . . . .	26
3.3 Comparisons with Parallel Stability Analysis . . . . .	33
<b>IV CONCLUSIONS . . . . .</b>	<b>37</b>
<b>REFERENCES . . . . .</b>	<b>38</b>

## LIST OF TABLES

1	Stability Criteria . . . . .	8
---	------------------------------	---

## LIST OF FIGURES

1	Instantaneous Flame Images . . . . .	2
2	Basic Combustion Instability Interactions . . . . .	3
3	Pressure Release Fluctuations Due to Flame-Vortex Interactions . . .	4
4	V-Gutter Flame Holder Array . . . . .	5
5	Schematic of Non-Reacting Wake of a Bluff Body . . . . .	6
6	Single Traveling Wave Instabilities . . . . .	8
7	Comparison of Absolute and Convective Instabilities Based on $\omega_{0,i}$ , $\omega_{i,max}$ and $\sigma$ . . . . .	8
8	Two Images from Same High Speed Video Show Evidence of Intermit- tency in Wake Structure . . . . .	12
9	Gabor Transforms at Given Location and Multiple Temperature Ratios	13
10	Experimental Rig . . . . .	15
11	Schematic of Test Section with Installed Bluff Body . . . . .	16
12	Sample of Experimental Design Parameters . . . . .	17
13	Tested Conditions Overlaid with 2D Parallel Flow Stability Map . .	18
14	Laser Set-Up . . . . .	19
15	Bluff Body Shapes . . . . .	20
16	Flame Edge Determined from Edge Tracking . . . . .	21
17	Spectra for Ballistic Bluff Body . . . . .	24
18	Spectral Engery vs Density Ratio . . . . .	25
19	Correlation Coefficient Between Top and Bottom Flame Edge Position	26
20	Comparison of Images to Show Intermittency . . . . .	27
21	Correlation Coefficient Between Time Signal and Sine Fit for Ballistic Bluff Body at 50 m/s and $x/D = 3.5$ . . . . .	29
22	Percentage of Time the Correlation Coefficient Exceeds the Threshold Value for the Ballistic Bluff Body at 50 m/s and $x/D = 3.5$ . . . . .	31
23	Effect of Density Ratio and Intermittency on Limit Cycle Amplitude for the Ballistic Bluff Body at 50 m/s and $x/D = 3.5$ and $\rho_t = 0.8$ . .	32

24	Dependence on Density Ratio of the Average Duration of the Times when $\rho_f > \rho_t$ for the Ballistic Bluff Body at 50 m/s and $x/D = 3.5$ and $\rho_t = 0.8$ . . . . .	33
25	$\omega_{0,1}D/U_{lip}$ Contours vs Axial Position and Density Ratio . . . . .	34
26	$v'_{RMS}$ vs Downstream Distance from the Predicted Maximum Abso- lute Instability Growthrate for Ballistic and V-Gutter Bluff Bodies at Multiple Density Ratios and Lip Velocities . . . . .	35
27	Predicted Growth rate vs measured intermittency for both bluff bodies and lip velocity . . . . .	36



## LIST OF SYMBOLS OR ABBREVIATIONS

$d$	Bluff body diameter.
$f_{BvK}$	Benard/von Karman instability frequency.
$f_{KH}$	Kelvin-Helmholtz instability frequency.
$p$	Pressure.
$Q_{1m}$	Nonsteady rate of heat release per unit mass of mixture.
$Re$	Reynolds number.
$St_D$	Struhoul number.
$T_b$	Temperature of burned products.
$T_u$	Temperature of unburned reactants.
$u_0$	Mean flow velocity.
$U$	Velocity field.
$U_{lip}$	Time-averaged axial velocity at bluff body trailing edge lip.
$v$	Velocity.
$x$	Location.
$X$	Observer velocity.
<b><i>Greek Characters</i></b>	
$\beta$	Backflow ratio.
$\gamma$	Specific heat ratio.
$\zeta$	Flame edge position.
$\rho_0$	Density.
$\rho_b$	Density of burned reactants.
$\rho_f$	Correlation coefficient between sine fit and original time signal.
$\rho_t$	Correlation coefficient threshold.
$\rho_u$	Density of unburned reactants.
$\rho_{U,L}$	Correlation coefficient between upper and lower flame edge positions .

$\sigma$	Temporal growthrate.
$\phi$	Streamwise eigenfunction.
$\Psi$	Stream function.
$\omega_{0,i}$	Absolute growth rate.
$\omega_{G,i}$	Imaginary component of global complex frequency.
$\omega_{i,max}$	Maximum temporal growthrate.

## SUMMARY

Safe operation of aircraft and aeroderivative industrial gas turbine engines relies heavily on the stability of the combustion process. Combustion instabilities are of interest because they may lead to harmful pressure oscillations and increases in temperatures within the engine that could be destructive to engine components. Fluid dynamics in the combustor directly affects combustion instabilities and is the subject of this research. The two types of hydrodynamic instabilities linked with combustion instabilities explored in this research are the Kelvin-Helmholtz and the Benard/von Karman instabilities. Previous research has shown that a high flame temperature ratio (the ratio between the temperature of the products and the temperature of the unburned reactants) suppresses the Von Karman street, allowing for the wake to be characterized by the higher frequency Kelvin-Helmholtz instability from which vortices are shed by the shear layers. However, at a low temperature ratio, the flame loses its ability to suppress the Von Karman instability. The result of the changing of wake structures is fluctuations in heat release and pressure, which can result in damaged hardware and loud audible tones. Research previously conducted in Georgia Tech's Ben T. Zinn Combustion Laboratory using chemiluminescence has given an approximation of the flow field disturbances caused by the Von Karman response by measuring flame response. The proposed research will utilize knowledge gained from previous flow field disturbance approximations and improve the approximations by using data acquisition hardware that will allow for the exact flow field to be measured. The purpose of this research is to demonstrate that hydrodynamic stability calculations can be used to predict the onset of the Benard/von Karman instability in bluff body flames.

# CHAPTER I

## INTRODUCTION

The objective of this research is to characterize the wake structure of a bluff body stabilized flame at intermediate temperature ratios. This research is motivated by the need for an improved understanding of the complex interactions between pressure, velocity, and heat-release oscillations that can result in combustion instabilities [10, 12, 14, 18, 20]. Bluff body flow is of particular interest due to the fact that bluff bodies are utilized in a variety of combustor applications for flame stabilization [9, 13, 15, 19]. Previous research has shown that the wake structure is affected by temperature ratio. While models have been created to examine intermediate temperature ratios, little is known about the transition from Kelvin-Helmholtz to Bernard/von Karman instabilities as temperature ratio is decreased. An improved understanding and ability to predict the onset of vortex shedding in bluff body flames is particularly important as the combustion instabilities can potentially compromise critical missions, in addition to destroying hardware [2, 12], leading to expensive and premature repairs or, in the most extreme cases, engine failure.

The research conducted will aid in characterizing the transition to and from the von Karman response through investigation of wake instability and von Karman suppression in an approximately two-dimensional bluff body flow field. The resulting data will be utilized to better understand how temperature ratio affects the physics of these phenomena.

## 1.1 *Combustion Instabilities*

Combustion instabilities occur in both aircraft and aeroderivative industrial engine combustors and pose a challenge for combustor designers [6]. When combustion instabilities occur, they are evident in pressure oscillations and heat release fluctuations [8, 16]. These heat release fluctuations excite acoustic waves which cause additional heat release fluctuations, creating a self-exciting feedback loop [4, 5, 6, 8]. The coupling between heat release and pressure oscillations is referred to as the Rayleigh criterion and sustains the oscillations. The resulting pressure oscillations can have frequencies that are close to or the same as the resonant frequencies of components causing vibrations in and damage to hardware [6]. Additionally, the pressure oscillations can create audible tones (also referred to as acoustic instabilities) that can compromise missions or create a hazardous environment for those working around the aircraft.

In addition to audible tones being a marker of combustion instabilities, the flame itself can be monitored for fluctuations in an experimental environment. The impact of the acoustic oscillations on the flame itself and the resulting fluctuations in heat release can be visualized in Figure 1 which shows two flame images, one of which shows a flame perturbed by acoustic oscillations for comparison [8].

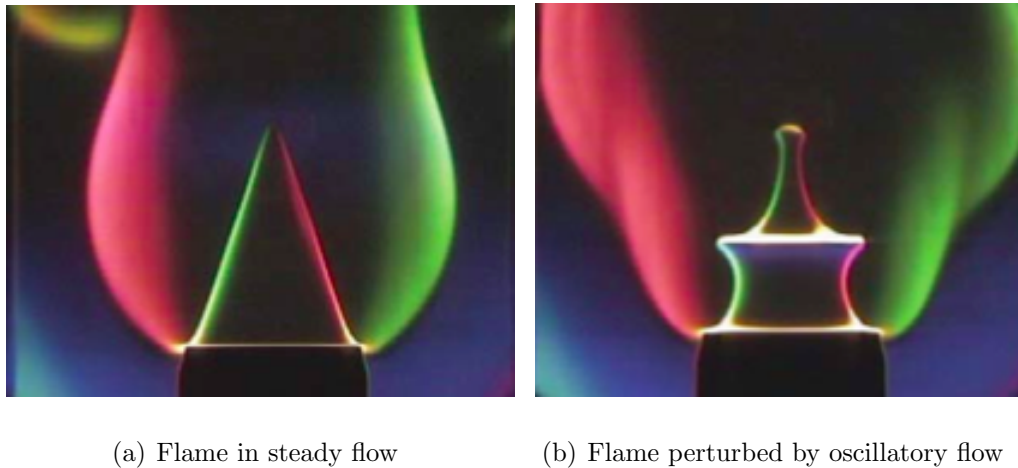


**Figure 1:** Instantaneous Flame Images

The effects of these oscillations of the flow include large amplitude structural vibrations, increased heat fluxes at the boundaries, flashback, flame blowoff, or, at worst, component failure [16].

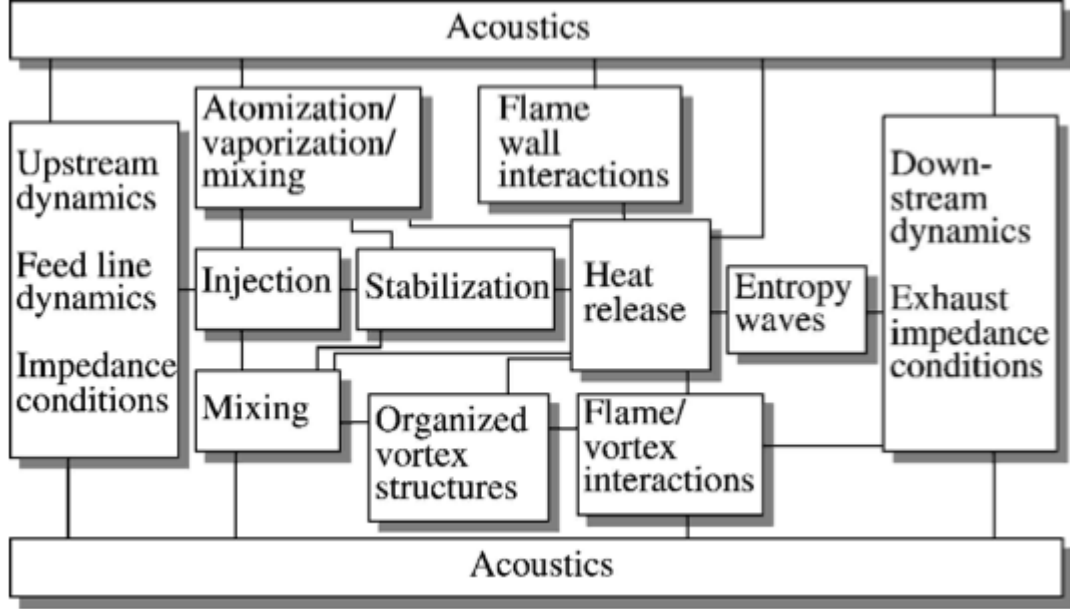


**Figure 2:** Basic Combustion Instability Interactions

The many potential interactions can be seen in Figure 2 from Decruix et al. [16], but for the sake of this proposal acoustic/flame coupling and flame-vortex interactions will be the interdependencies explored most thoroughly.

### 1.1.1 Acoustic/Flame Coupling

Acoustic/flame coupling refers to the interactions between acoustic oscillations and the heat release from the flame. In order to relate the acoustic instabilities with the combustion instabilities, a wave equation

$$\frac{\partial v_1}{\partial t} = \frac{1}{\rho_0} \nabla p_1 \quad (1)$$

where  $v$ ,  $\rho_0$ , and  $p$  are velocity, density, and pressure, respectively, is used. Additionally, an acoustic source term, as a result of chemical reactions, is introduced

$$(\gamma - 1) \frac{\partial Q_{1m}}{\partial t} \quad (2)$$

where  $\gamma$  and  $Q_{1m}$  are used to relate the pressure field to heat release and turbulence. These equations are only valid under the assumption of low Mach number, which is reasonable for the flow velocities that will be used in the proposed experiments. While these equations are simplified by neglecting terms based on order of magnitude and neglecting acoustic instabilities due to aerodynamics, the equations successfully show that the rate of change of heat release fluctuations can drive pressure waves resulting in damaging acoustic tones.

### 1.1.2 Flame-Vortex Interactions

Vortices (which will be discussed in further detail in subsequent sections) can drive a variety of types of combustion instabilities. High frequency oscillations can create large fluctuations in velocities near the flame holder, triggering the vortex shedding [21]. The vortices transport fresh gases downstream where they will combust and create a heat pulse, further exciting the acoustic oscillations [21]. Additionally, vortex structures lead to rapidly changing flame area resulting in heat release fluctuations [16]. In essence, this unsteady combustion and resultant heat release fluctuations lead to the damaging acoustic waves [4]. The concept of flow perturbations leading to heat release fluctuations and ultimately to acoustic waves can be visualized in Figure 3 [16].

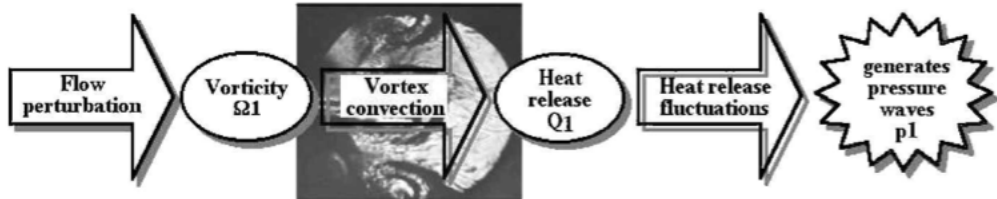


**Figure 3:** Pressure Release Fluctuations Due to Flame-Vortex Interactions

The concept of vortex-flame interaction is fundamental to the proposed research as the transition between the von Karman vortex street and Kelvin-Helmholtz vortex dominated bluff body stabilized flame that will be the subject of this project. An improved understanding of the transition between the two different vortex dominated wakes as temperature ratio varies will ultimately contribute to the improved design of combustors leading to reduced damage due to combustion instabilities.

## ***1.2 Bluff Body Flows***

Combustion instabilities pose a challenge for all combustor configurations. However, this research will focus solely on combustors that utilize bluff bodies to stabilize the flame. Bluff bodies are often used in an array (an example can be found in Figure 4).



**Figure 4:** V-Gutter Flame Holder Array

A variety of bluff body arrays are utilized, but for the purpose of this research only one bluff body will be placed in the test section at a given time as the focus of the research is to study the fundamental physics of a bluff body stabilized flame and this can best be accomplished by using only one bluff body. Surrounding this bluff body, three fundamental regions of the flow field exist: boundary layers, separated shear layers, and the wake [11, 18, 19, 20]. These regions exist in both non-reacting and reacting flows. In reacting flows, the region of slower moving air (wake) is where the flame exists [13, 18]. This region of recirculation and wake is created by vortex



shedding from the bluff body. Additionally, an inflexion point occurs in the velocity field of the separated shear layer and the wake, leaving both easily affected by hydrodynamic instabilities [20].

### 1.2.1 Hydrodynamic Instabilities

The two types of hydrodynamic instabilities of interest in this research are the Kelvin-Helmholtz (KH) and Benard/von Karman (BvK) instabilities. KH vortices characterize the shear layer [18, 20]. The vortex pairs, which are controlled by the convective KH instability, are of opposite sign and are symmetrically shed at a higher frequency [18, 20]. In contrast, the BvK absolute instability is characterized by alternating vortex shedding [18, 20] and a frequency,  $f_{BvK}$  that is non-dimensionalized by  $St_D$  which scales to  $u_0$  over  $d$  through the following relation

$$f_{BvK} = St_D * u_0 / d \quad (3)$$

where  $St_D$  is independent of  $Re$  for a given range of  $St_D$  values dependent on the bluff body geometry. For high Reynolds numbers, the following relation holds true

$$f_{KH} = 0.0235 * f_{BvK} * Re^{0.67} \quad (4)$$

illustrating that the KH frequency,  $f_{KH}$ , is much larger than the  $f_{BvK}$  [18, 20]. A comparison of the shear layer and wake of a non-reacting flow can be seen in Figure 5, which is reproduced from Prasad and Williamson [11].

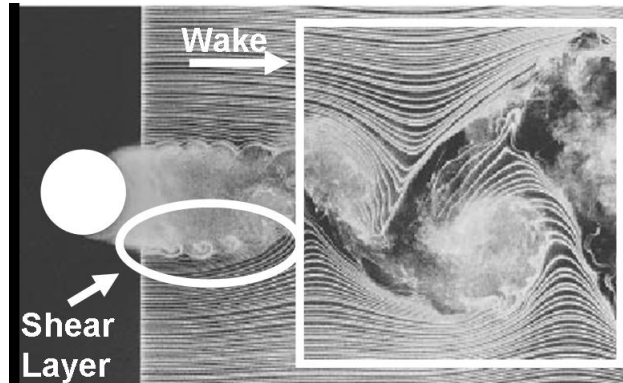


**Figure 5:** Schematic of Non-Reacting Wake of a Bluff Body

This image shows that, while the  $f_{KH}$  is much larger than the  $f_{BvK}$ , the magnitude of the BvK instability is much larger than the KH instability.

There has been a significant amount of research in non-reacting flows. However, the flow field changes substantially between non-reacting and reacting flows. The work conducted in studying the bluff body wake structures in reacting flow has only been performed at high or low temperature ratios, but little has been done to study the intermediate temperature ratios in which the wake structure transitions between KH and BvK instabilities.

An improved understanding of this transition is particularly relevant to the reduction of combustion instabilities. The transition between the two instabilities causes large changes in heat release and pressure gradients due to the amplitude and frequency differences between the two types of instabilities. Therefore in order to better design for and control these instabilities, particularly the BvK instability that can facilitate and excite combustion instabilities, the transition between the two must be better understood.

### **1.2.2 Absolute and Convective Instabilities**

This research will explore two main categories of instabilities. A local instability is an instability in the local velocity profile, while a global instability occurs throughout the entire flow field [7]. A locally absolute instability is characterized by an instability that affects the entire flow, with the disturbances remaining at the original source [7]. Alternatively, a locally convective instability, such as the KH instability is one in which the disturbances are carried downstream [7]. Huerre and Monkewitz [7] illustrate the aforementioned instabilities in addition to other typical impulse responses as seen in Figure 6.

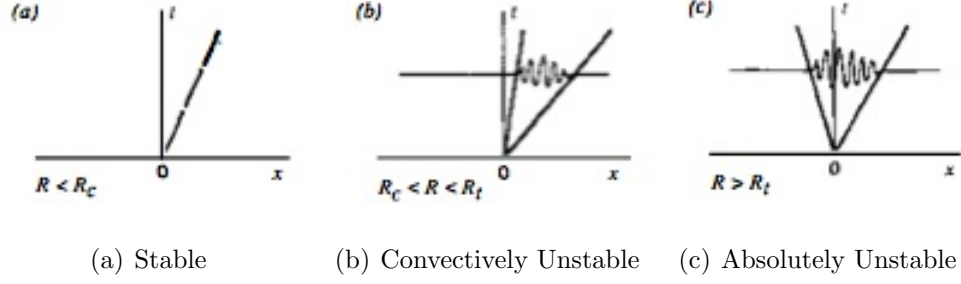


**Figure 6:** Single Traveling Wave Instabilities

Stable flow, absolutely unstable flow and convectively unstable flow can be differentiated from one another based on the criteria listed in Table 1 and displayed in Figure 7.

**Table 1:** Stability Criteria

$\omega_{i,max} > 0$	$\omega_{0,i} > 0$	Absolutely Unstable
$\omega_{i,max} > 0$	$\omega_{0,i} < 0$	Convectively Unstable
$\omega_{i,max} < 0$	$\omega_{0,i} < 0$	Stable

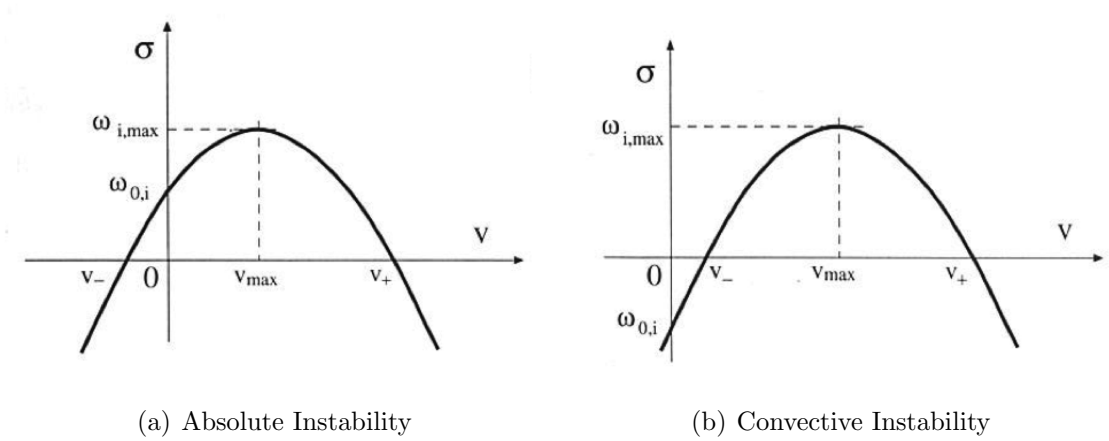


**Figure 7:** Comparison of Absolute and Convective Instabilities Based on  $\omega_{0,i}$ ,  $\omega_{i,max}$  and  $\sigma$

In order to not only characterize local instabilities, but also global wake and global instabilities, the differences between globally stable and unstable flow must be

established. Huerre and Monkewitz state that global stability can be defined using the following equations. The first equation is

$$\Psi(x, t; X) = \Phi(x; X)e^{-i\omega_G t} \quad (5)$$

where  $\Psi$ ,  $\phi$ ,  $x$ , and  $X$ , are stream function, streamwise eigenfunction, location, and observer velocity, respectively, is derived from Rayleigh's Equation, which can be seen below. Rayleigh's Equation defines the flow field through

$$\phi'' - k^2\phi - \frac{U''(y)}{U(y) - c}\phi = 0 \quad (6)$$

where  $U$  is the velocity [1, 7]. The second pair of equations:

$$\begin{aligned} \text{globally stable flow: } \omega_{G,i} &< 0 \\ \text{globally unstable flow: } \omega_{G,i} &> 0 \end{aligned} \quad (7)$$

define global stability based on the imaginary component of the global frequency,  $\omega_{G,i}$  [7]. The analysis of data as a result of the research conducted will capitalize on this method of determining stability and instability in addition to using methods to differentiate between the types of instabilities that are occurring in the reacting flow behind the bluff body.

### ***1.3 Reacting Flows***

Reacting flows influence the bluff body wake in ways that are not observed in non-reacting flows. The wakes of non-reacting flows are characterized by the von Karman vortex street [10, 13, 15]. However, reacting flow varies greatly from non-reacting flow in that exothermicity influences the shear layers and wake flow, affecting flow stability [13, 15, 19]. These reacting flows tend to have reduced vorticity magnitudes and turbulence intensities [19]. Additionally, these flows have a gas dilatation ratio ( $\rho_u/\rho_b$ ) [19] greater than one, unlike non-reacting flows which have a gas dilatation ratio of one, introducing effects as a result of density gradients [18]. Among these effects

are baroclinic velocity and the torque resulting from this velocity [19]. Baroclinic torque creates a vortical component as a resultant of misaligned pressure and density gradients and contributes to the vorticity [18]. The phenomena of the suppression of shear layer vorticity due to competition between shear layer and baroclinic vorticity leading to the BvK instability emerging as the dominant instability will be explored through this research to further characterize the effects of temperature ratio on bluff body stabilized flame wake.

### **1.3.1 Wake Structure**

In reacting flows, temperature ratio strongly affects the strength of wake instability. The temperature ratio of interest is the ratio of the temperature of products and reactants in the test section ( $T_b/T_u$ ). It has been found that at high temperature ratios ( $T_b/T_u$  greater than 3.5) the dilatation and baroclinic torque will suppress the von Karman vortex street, making the wake dominated by KH instabilities. In contrast, at low temperature ratios ( $T_b/T_u$  less than 1.5), the wake is dominated by BvK instabilities. There has, however, been limited experimental research conducted on the wake structure at intermediate temperature ratios. The research conducted will aim to help better understand wake structures and the transition from KH to BvK instabilities at intermediate temperature ratios. This research is particularly important as the transitions from KH to BvK instabilities can facilitate the acoustic tones of interest. The research will contribute to a better understanding of wake structure at intermediate temperature ratios, leading to improved designs and controls and ultimately a decrease in damage due to the acoustic tones occurring within the range of interest.

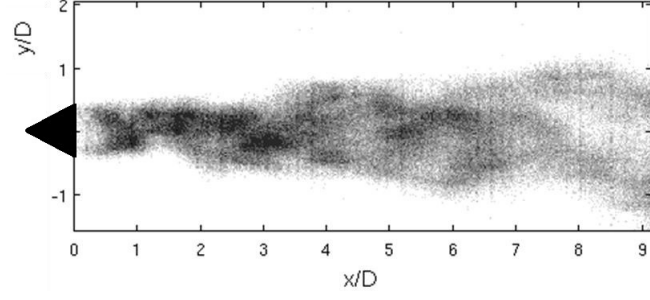
### **1.3.2 Flame Stabilization**

In bluff body stabilized flows, the flame can remain anchored as long as there remains a re-circulation zone behind the bluff body in which the combustion products mix

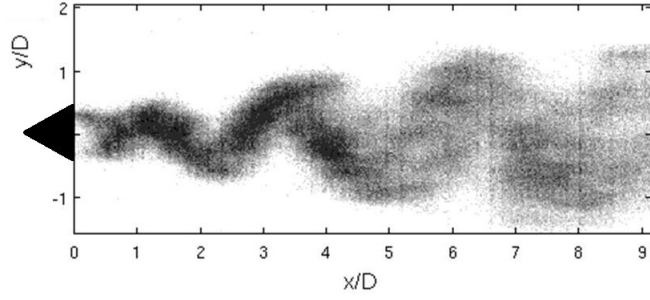
with and ignite the unburnt mixture within the shear layers [9]. Blowoff occurs when the velocity of the flow is such that there is insufficient re-circulation to hold the flame and is a function of flow velocity, stoichiometry, vitiation levels, pressure, temperature, blockage ratio, and bluff body shape [19]. In addition to potentially leading to the extinguishing of the flame when the combustor is operating near blow off limits, it has been found that operating near these points increased the presence of the BvK instability [9, 17]. In order to prevent this cause of BvK instabilities, no tests will be conducted near blow off limits.

## **1.4 *Summary***

Vortex shedding will occur in both non-reacting and reacting flows. Research conducted has shown that at intermediate temperature ratios, the wake structure alternates between KH and BvK instabilities, with BvK instabilities being present for increasing percentages of time as the temperature ratio is lowered as can be seen in Figure 8 [3].



(a) KH Dominated



(b) BvK Dominated

**Figure 8:** Two Images from Same High Speed Video Show Evidence of Intermittency in Wake Structure

This phenomenon is also evident in Figure 9, which displays plots of the results of Gabor transforms on the data exhibit. The clear band that begins to develop at the expected  $f_{BvK}$  as temperature ratio is lowered reinforces that the time spent in the von Karman instability increases as temperature ratio decreases.

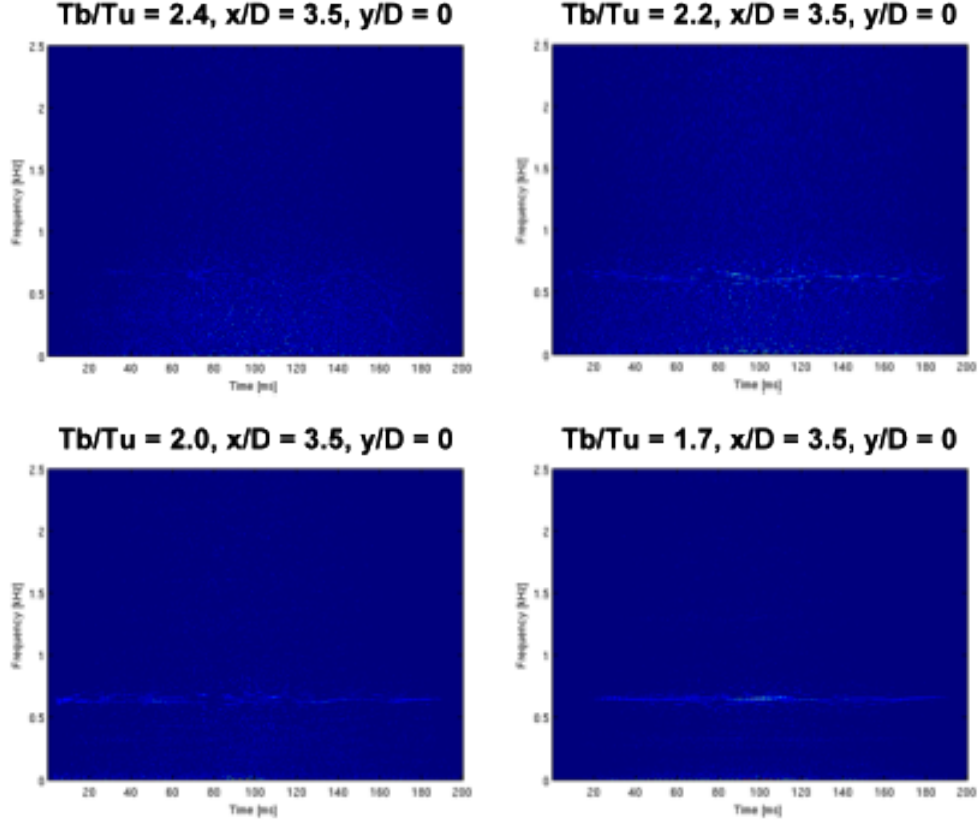


**Figure 9:** Gabor Transforms at Given Location and Multiple Temperature Ratios

The plots demonstrate that the BvK instability becomes increasingly more present in atmospheric premixed methane flames at temperature ratios lower than 2.4. The knowledge gained is critical to the overall understanding of wake structure in reacting bluff body flows due to the fact that the BvK instabilities are at a frequency within the range of frequencies at which the acoustic tones of interest occur. The results of the high speed video and Particle Image Velocimetry analysis, including the Gabor transforms, leads us to believe that the dominance of instability in the wake structure is not simply a one time transition from one type to the other. The knowledge gained from this analysis is critical to the overall understanding of wake structure in reacting bluff body flows due to the fact that the BvK instabilities are at a frequency within the range of frequencies at which the acoustic tones of interest occur. With the knowledge of the intermittency of the transitions between wake structures, we have



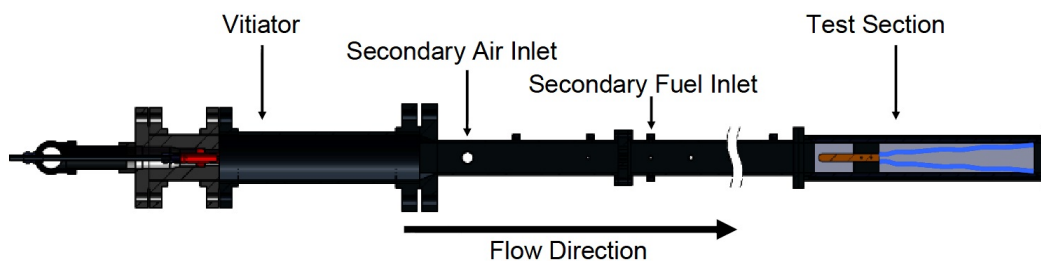
a better understanding of wake structures at intermediate temperature ratios but are still currently unable to predict the onset of the BvK instability. The ability to predict the onset of the BvK instability will ultimately aid in the reduction of acoustic tones associated with the pressure fluctuations due to the coupling of combustion and acoustic instabilities. The reduction in these tones can occur through improved design leading potentially to reduced frequency of repair due to damage caused by the acoustic tones of interest. The research conducted will compare various conditions, including variations of temperature ratio, lip velocity, and bluff body shape in order to characterize bluff body wakes and ultimately demonstrate aid in the characterization of the bluff body wake at intermediate temperature ratios.

## CHAPTER II

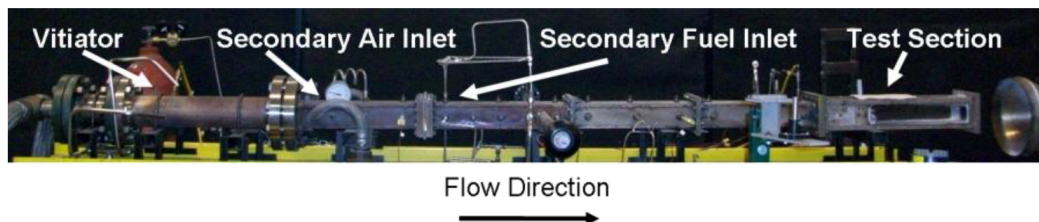
### MATERIALS AND METHODS

#### 2.1 *Experimental Facility*

The experimental set-up consists of two premixed methane burners in series as can be seen in Figure 10.



(a) Rig Schematic



(b) Rig Photo

**Figure 10:** Experimental Rig

The first combustor heats and vitiates the flow prior to it reaching the second combustor. Primary air and fuel are premixed and can be controlled independently of the secondary fuel and air, which directly precede the secondary burner. The downstream combustor is the afterburner, with four quartz walls to allow optical access. A bluff body is fixed upstream of the quartz windows such that the trailing edge of the body is at the beginning of the quartz window. The bluff body, as can be seen in Figure 11, spans the width of the test section to create a nominally 2-D flow.

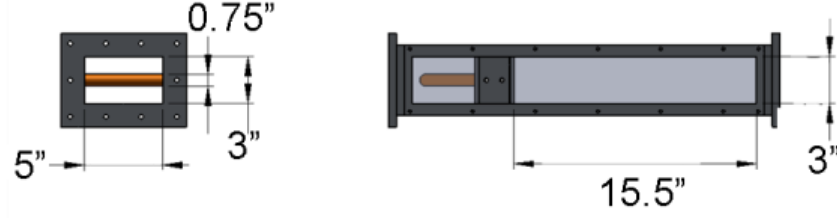


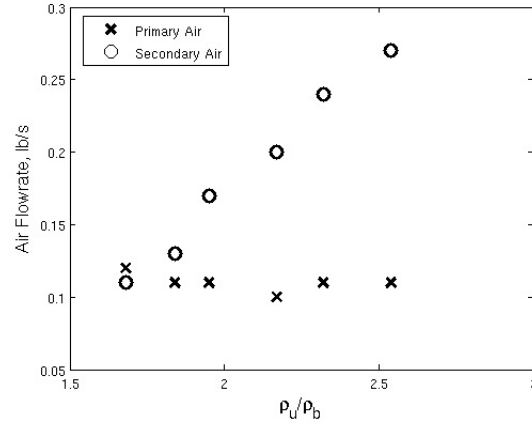
**Figure 11:** Schematic of Test Section with Installed Bluff Body

Flow velocity and temperature ratio across the afterburner flame can be varied by adjusting both air and fuel flow rates. The mass flow rates are measured across calibrated knife-edge orifice plates using the static pressure transducers and Omega PX771A differential pressure transmitters. Additionally, the temperature upstream of the vitiator is measured using a type K thermocouple and Omega TX13 Smart Temperature Transmitter. Uncertainty analyses were performed on the thermocouple readings as well as the air and gas flow rates for the various test conditions. The thermocouple readings were found to have an uncertainty of less than 1%. For the 50 m/s case the uncertainty was approximately 2% for the measured gas flow rates and the resulting temperature and density ratios and for the 20 m/s case the uncertainty was approximately 4% for the measured gas flowrates and approximately 9% for the resulting density ratios. For the uncertainty analyses of the air velocity measurements, the flowrate measurements were compared to the Particle Image Velocimetry (PIV) measurements and the differences were found to be 6 m/s for the 50 m/s cases and 0.6 m/s for the 20 m/s case.

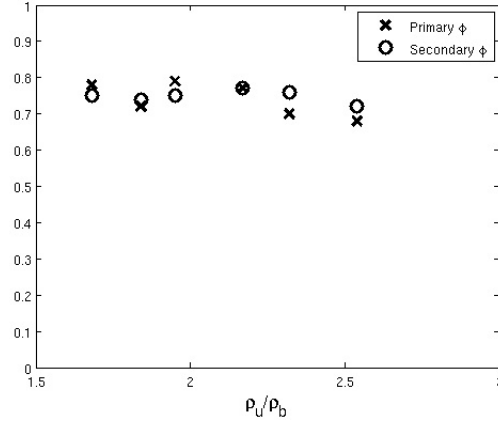
Additionally, the flow in the test section is longitudinally acoustically forced at the combustor's resonant frequencies to further simulate the acoustic environment in a real-world combustor.

## 2.2 Test Conditions

Test matrices are constructed such that a given test will have approximately the same lip velocity while changing the air flow rates and equivalence ratios to test at a range of density (or temperature) ratios. An example of the airflow rates and equivalence ratios for the various density ratios for a 50 m/s ballistic bluff body test can be seen in Figure 12.



(a) Airflow Rates



(b) Equivalence ratios

**Figure 12:** Sample of Experimental Design Parameters

Actual test conditions can be seen in Figure 13 which displays the backflow ratio overlayed with the absolute stability map created by Huerre and Monkewitz [7].

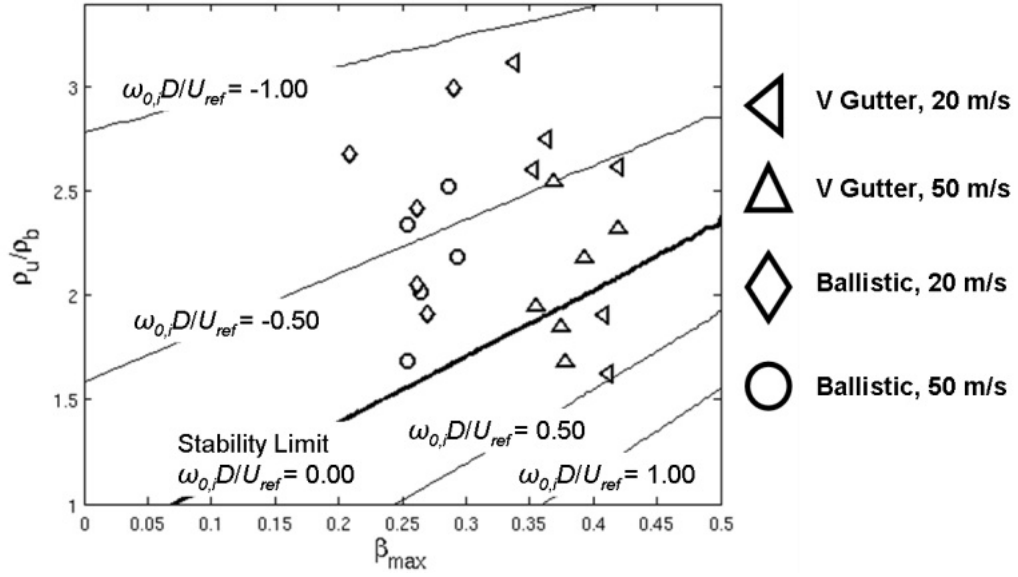


**Figure 13:** Tested Conditions Overlaid with 2D Parallel Flow Stability Map

It can be seen from the overlay of the test points on the stability map that the tests were designed in order to collect data points in theoretically both the convective and absolutely unstable regime. This was able to be achieved by implementing the use of a v-gutter for testing in addition to the ballistic bluff body.

### 2.3 Diagnostic Equipment

Multiple methods are employed to conduct data acquisition. The first method is high speed chemiluminescence, utilizing a Photron Fastcam SA3 camera with BG-28 optical filter capturing images at 3,000 frames per second with a resolution of 512 x 256 pixels. A BG-28 filter is placed between the camera lens and test section, which aids in eliminating light transmitted to the camera due to black body radiation with the filter transmission exceeding 10% for wavelengths between 340 nm and 630 nm with a peak of 82% transmission at 450 nm. High speed chemiluminescence was only captured for the ballistic bluff body.

The second method of data acquisition is performed using PIV. PIV is a non-intrusive

optical technique using a laser sheet to study the flow field in a time resolved manner. The PIV system used is a LaVision Flowmaster Planar Time Resolved system paired with a Litron Lasers Ltd. LDY303He: Nd:YLF laser with a wavelength of 527 nm and 5 mJ/pulse pulse energy at a frequency of 10 kHz. Additionally, the camera used is a Photron HighSped Star 6 camera which has a 640 x 448 pixel resolution with 20 x 20 micron pixels on the sensor at a 10 kHz frame rate.

This set-up for PIV relative to the test section can be seen in Figure 14.

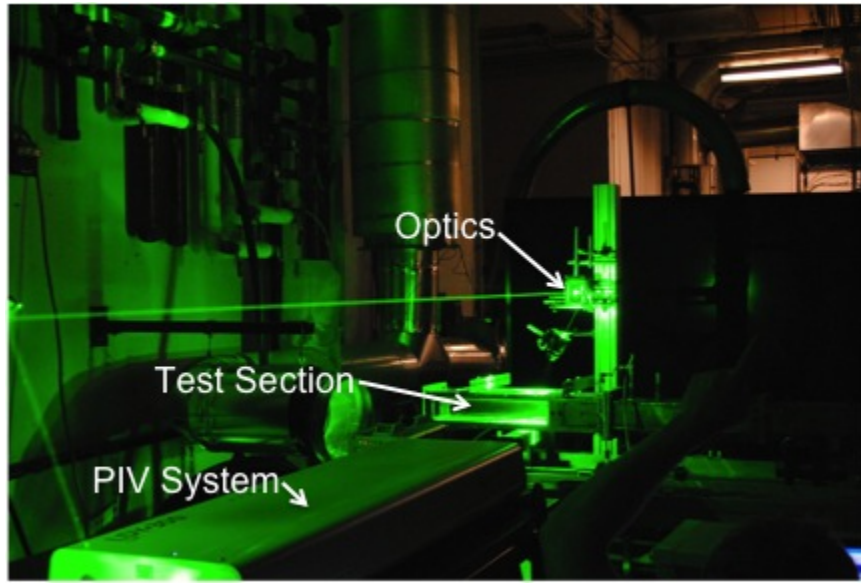


**Figure 14:** Laser Set-Up

In order to obtain data, the two lasers each pulse at a frequency of 10,000 Hz with the high speed camera capturing each pulse in a separate frame with 12  $\mu$ s between image pairs. Aluminum oxide ( $Al_2O_3$ ) particles approximately  $2\mu$ m in diameter are injected into the flow upstream of the combustor and are detected by the camera. The pairing of two sequential images, as a result of the paired laser pulses, allows for a time resolved analysis of the flow field and a direct calculation of velocities within the flow field. Additionally, the field being imaged can be adjusted so that both zoomed in and zoomed out images can be taken to focus on either the structure of the wake

immediately after the bluff body or the wake structure further downstream. Prior to conducting the PIV test, the flow conditions are recorded once every second for ten seconds and then averaged to be used during data analysis of the PIV results. PIV was conducted for both the ballistic bluff body and the v-gutter bluff body at the same test conditions used for high speed chemiluminescence.

## 2.4 *Bluff Body Variation*

Two different bluff bodies will be used for PIV testing and flow structure analysis as can be seen in Figure 15.

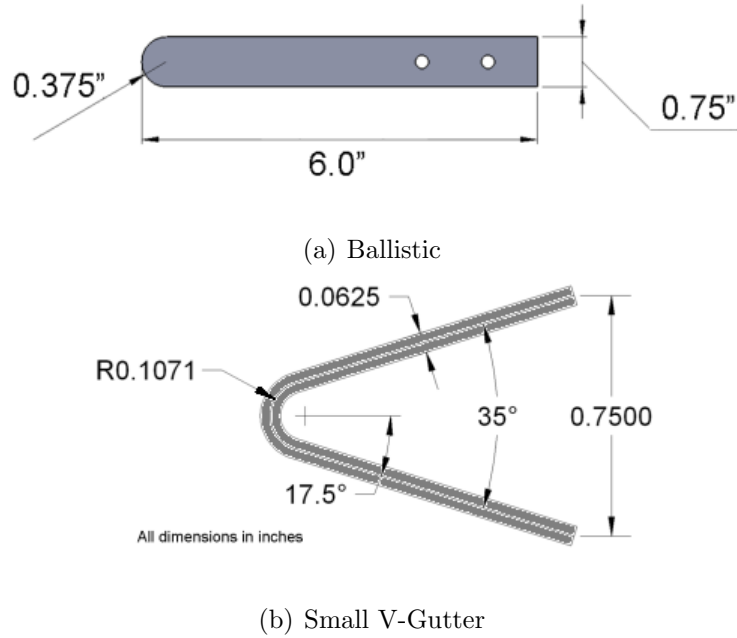


**Figure 15:** Bluff Body Shapes

The first bluff body is the ballistic shape, which has been used in previous experiments conducted for studying bluff body wakes in the Combustion Lab. This shape is chosen due to its basic geometric properties. In order to vary the backflow ratio, which is a factor in the theoretical prediction of absolute versus convective instability of the wake (as seen in figure 13), the second bluff body shape used was a v-gutter. In addition to the v-gutter having a different backflow ratio, it also is the shape that

would be more commonly found in real-world combustors.

## 2.5 Data Analysis

Two sources of data, high speed video and PIV will be analyzed using MATLAB. PIV also utilizes the DaVis 7.2 software from LaVision, which will be discussed in further detail the PIV section.

### 2.5.1 High Speed Video

From high speed video, the flame edge can be calculated and tracked in order to determine the flame edges as a function of time as can be seen in Figure 16.

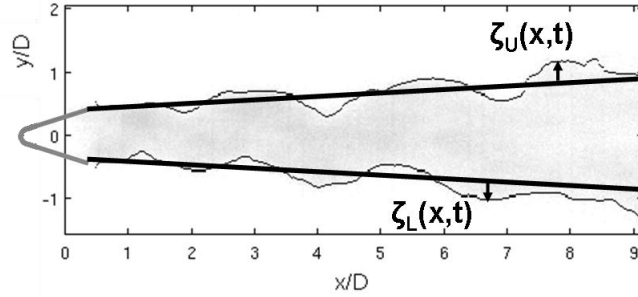


**Figure 16:** Flame Edge Determined from Edge Tracking

Discrete Fourier transforms can then be performed on the flame edge in relation to time to determine spectrum of the flame edge response at a given location,  $\zeta$ . The two flame edges can also be compared in order to determine the correlation between the two flame edges,  $\rho_{U,L}$ , computing whether the two edges are fluctuating symmetrically or sinusoidally. It was noted in observing the data that due to the differences between the signals of KH and BvK instabilities, the signal during von Karman dominance appears periodic while the time during which KH is dominant the signal appears as noise. A sine fit will be conducted on the signal in order to approximate the amount of time the wake is characterized by von Karman vortex street and quantify the percentage of time the BvK instability is dominant as a function of temperature ratio.



### 2.5.2 PIV

PIV allows for a direct measurement of the flow field and thus, presumably, a better understanding of the fluid dynamics of the wake. Prior to data analysis in MATLAB, the DaVis software is used to process the PIV data by performing background subtraction and calculating the velocity fields. The velocity field data can then be imported to MATLAB to be analyzed. Gabor transforms will be performed on velocity time histories to visualize the intermittency of the transition from KH instability to BvK instability by plotting frequency versus time. While the data from high speed video could only be analyzed for percentage of time the wake was characterized by the BvK instability through sine fit estimations, this same percentage of time can be directly calculated using PIV data in order to better estimate the temperature ratio, which appears to be the maximum for which the BvK instability is dominant.

## CHAPTER III

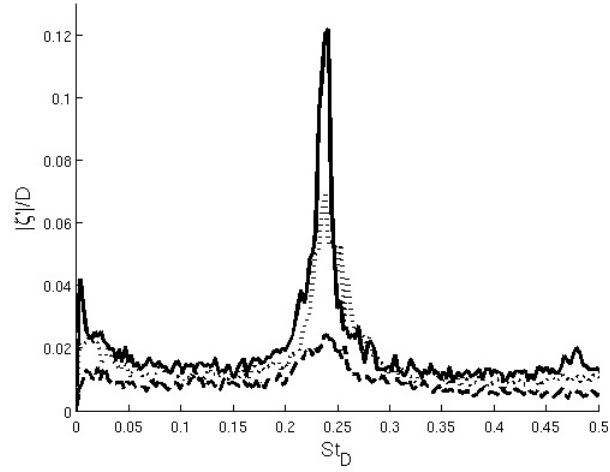
### RESULTS AND DISCUSSION

This section will show results from and discuss multiple characteristics of the flame and flow dynamics of the bluff bodies investigated.

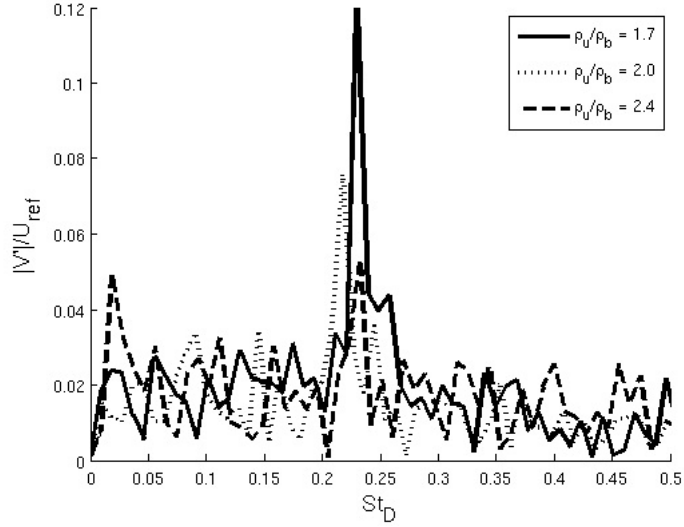
#### *3.1 Spectral and Correlation Analysis*

Flame and flowfield dynamics were quantified using high speed chemiluminescence videos and PIV, respectively. In order to quantify flame dynamics using high speed videos, the traverse position of the top and bottom flame branches were found as a function of axial position and time using edge tracking; an example of edge tracking can be seen in Figure 16. It is important to note from the image that the axis are defined such that there is a positive displacement when the flame edge value is greater than the mean value. The mean flame edge location of the top and bottom flame branches independently by averaging the flame edge location for each video (thus a different mean edge location was found for each video and condition). The edge tracking results in a time series for each flame branch of the edge positions at each axial position. The results were then Fourier transformed to determine the temporal spectra.

A corresponding analysis of the flowfield dynamics was performed utilizing PIV data. From the PIV data, a spectrum was produced by using the transverse centerline velocity  $v'(x, y = 0, t)$  and the Fourier transform of the centerline velocity  $v'(x, y = 0, f)$ . A comparison of two spectra, one resulting from the flame edge tracking and one resulting from the PIV data analysis, for a ballistic bluff body at 50 m/s and three different temperature ratios can be seen in Figure 17.



(a) Upper Flame Edge from High Speed Video



(b) Centerline Transverse Unsteady Velocity Magnitude from PIV

**Figure 17:** Spectra for Ballistic Bluff Body

The spectra show that at higher temperature ratios, the spectrum is broad band, with a small peak beginning to appear around a  $St_D$  of 0.24. However, as the temperature ratio is decreased, a narrowband peak appears and grows about a Strouhal number of 0.24. The peak forming around this value is particularly significant as a value of 0.24 is the value that correlates to the frequency of BvK vortex shedding. To further investigate the characteristics of the spectra, particularly in the region

of frequencies near the peak response, the integrated power under the spectral peak from Strouhal number 0.20 to 0.28 as a function of density ratio was calculated. The computed power was then converted to a root mean square (RMS) of the signal at the peak frequency by way of Parseval's theorem and using the relation seen in the following equation

$$s_{rms} = \sqrt{\frac{1}{T} \int_{f^-}^{f^+} |\Phi(f)|^2 df} \quad (8)$$

which related the RMS of the time series  $s(t)$  of duration  $T$  and spectrum  $\Phi(f)$ . The RMS values calculated can be seen in Figure 18.

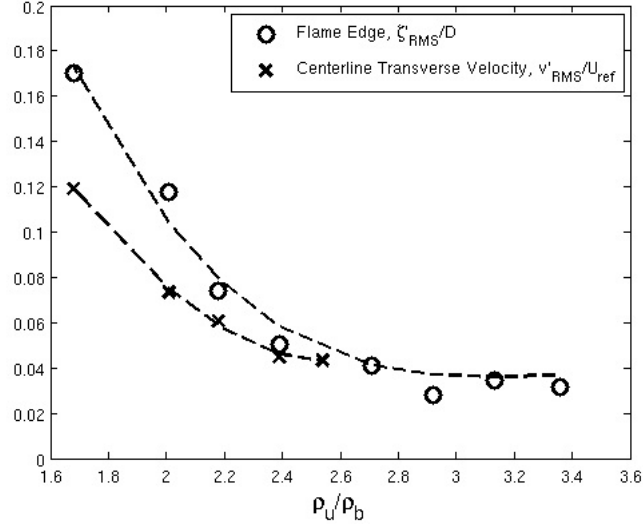


**Figure 18:** Spectral Engery vs Density Ratio

This figure illustrates the similarities between the flame and flow data with the data being in close proximity. Additionally, it can be seen that as the density ratio is lowered, the RMS values increases demonstrating that the percentage of time that the BvK instability is dominant increases as the density ratio is lowered.

The underlying flow structures creating perturbations to the flame branches can be better understood by calculating the correlation coefficient between the two flame branches. A positive correlation coefficient corresponds with a symmetric flame,

while a negative correlation coefficient corresponds with an asymmetric flame. A correlation coefficient of approximately zero indicates that the disturbances to the flame are uncorrelated and much smaller than their transverse separation distance. The correlation coefficient data for the ballistic bluff body at 50 m/s can be seen in Figure 19

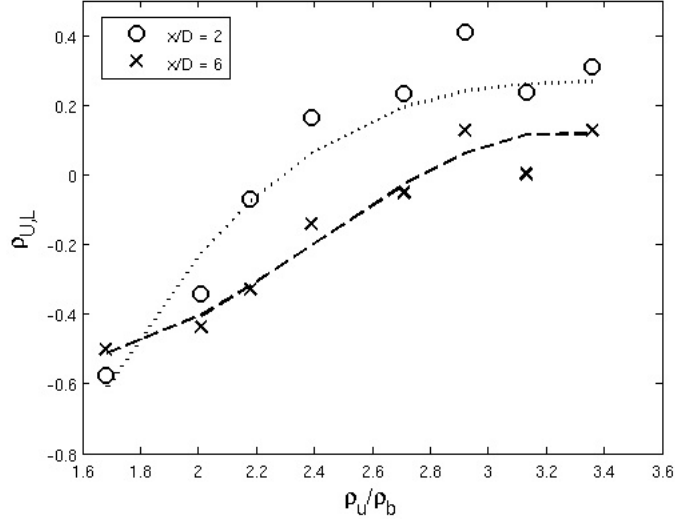


**Figure 19:** Correlation Coefficient Between Top and Bottom Flame Edge Position

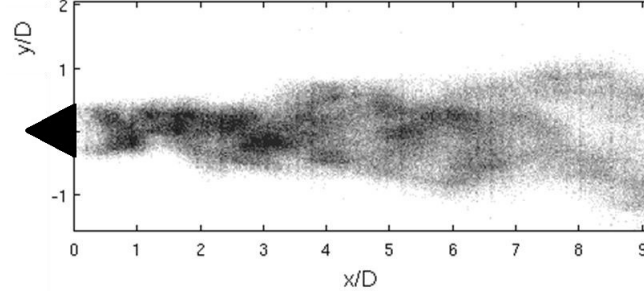
In summary, Figure 17 suggests that at low density ratios, the flow evolved into an absolutely unstable flow. This is supported in Figures 18 and 19 which show that there is a gradual increase in spectral energy at the asymmetric vortex shedding frequency, as well as a gradual increase in asymmetry and large scale structures in the wake.

### 3.2 Intermittency

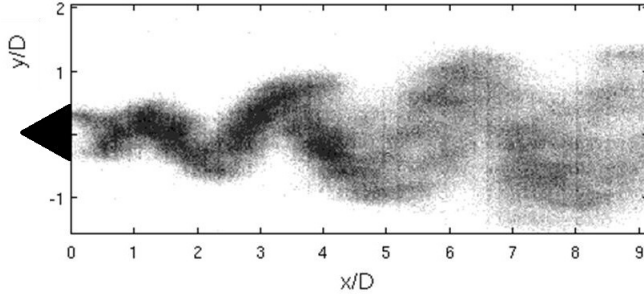
In order to verify that the increasing power in the narrowband fluctuations were due to the BvK instability being dominant for a larger total percentage of time and not simply due to the gradual growing amplitude of the instability, intermittency was confirmed visually through comparison of images from high speed video and quantified

using moving sine wave fitting.

An example of intermittency can be seen by comparing the following two images in Figure 20, from the same operating conditions, occurring at only a fraction of a second apart.



(a) KH Dominant



(b) BvK Dominant

**Figure 20:** Comparison of Images to Show Intermittency

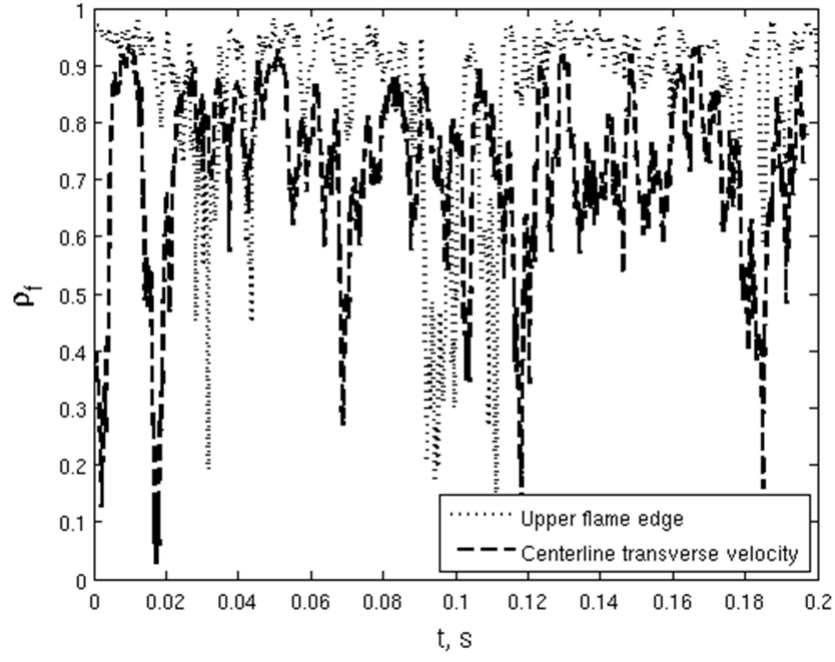
It can be seen from these images that the top image shows a flame lacking a clear coherent structure, while the bottom image shows a flame with a clear structure demonstrating intermittency.

Intermittency was quantified by locally fitting a sine wave to the time series in two period windows. The frequency of the sinusoidal fluctuation was fixed to  $f_0 = 0.24U_0/D$  which corresponds to a frequency of approximately 630Hz. The correlation coefficient,  $\rho_f$  defined as

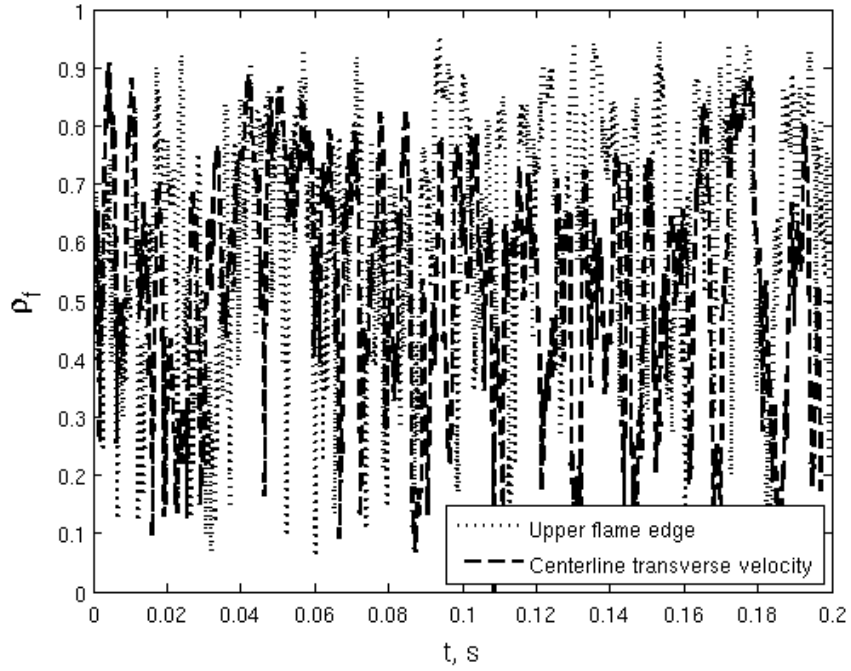
$$\rho_f(x) = \frac{\zeta_U(x, t) \sin(2\pi f_0 t)}{\sqrt{(\zeta_U(x, t)^2)(\sin(2\pi f_0 t))^2}} \quad (9)$$

was calculated for the fit and the actual data for each of the windows.

The calculated correlation coefficient for each window was then plotted with respect to time for both the upper flame edge and the centerline transverse unsteady velocity for the various temperature ratios and can be seen in Figure 21.



(a)  $T_u/T_b = 1.7$

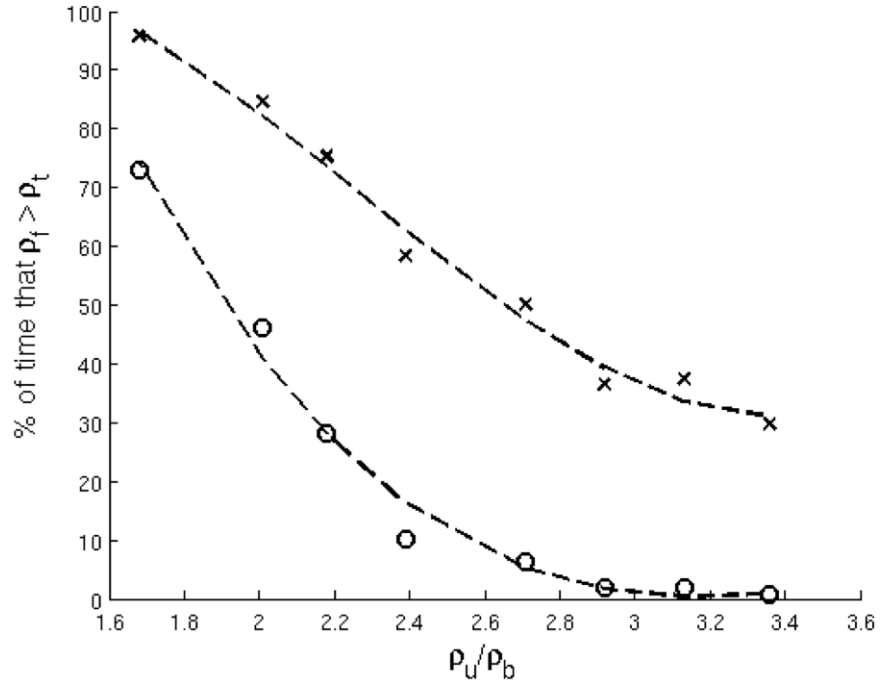


(b)  $T_u/T_b = 2.4$

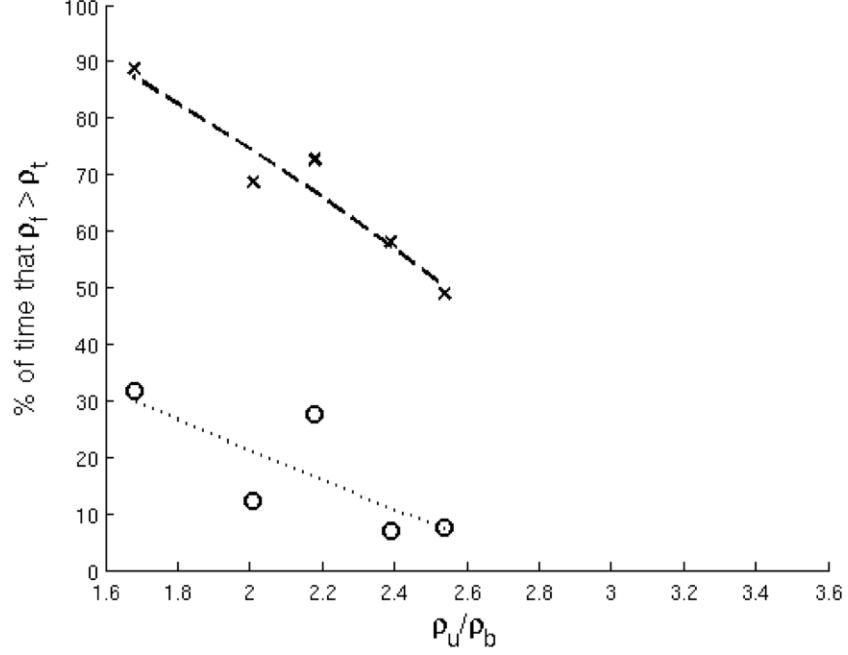
**Figure 21:** Correlation Coefficient Between Time Signal and Sine Fit for Ballistic Bluff Body at 50 m/s and  $x/D = 3.5$



It is evident that at a lower temperature ratio,  $\rho_f$  spends a significant portion of the time between 0.8 and 1.0, indicating the sinuous mode is dominant for a larger fraction of the time. It can also be seen that as the temperature ratio increases, the fraction of time  $\rho_f$  spends between 0.8 and 1.0 decreases. Two threshold values were investigated and plotted to demonstrate that as the threshold ( $\rho_t$ ) was decreased from 0.8 to 0.5, the overall trend is maintained. These results were summarized visually in Figure 22.



(a) Upper Flame Edge (Chemiluminescence)



(b) Centerline Transverse Unsteady Velocity (PIV)

**Figure 22:** Percentage of Time the Correlation Coefficient Exceeds the Threshold Value for the Ballistic Bluff Body at 50 m/s and  $x/D = 3.5$

It can be seen that as density ratio, and thus temperature ratio, increases, the fraction of time the sinusoidal fit is above the threshold increases. This brought about the inquiry into the amplitude of the sinuous mode and how much of the growth in amplitude is due to intermittency effects along with how much of the growth in amplitude can be attributed to a rise in limit cycle amplitude.

The conditional amplitude of the sine fit averaged over time periods during which the correlation coefficient between the sine wave and fit was greater than the threshold value, denoted by  $\zeta(\rho_f > \rho_t)$  was calculated. The resulting values can be seen in Figure 23.

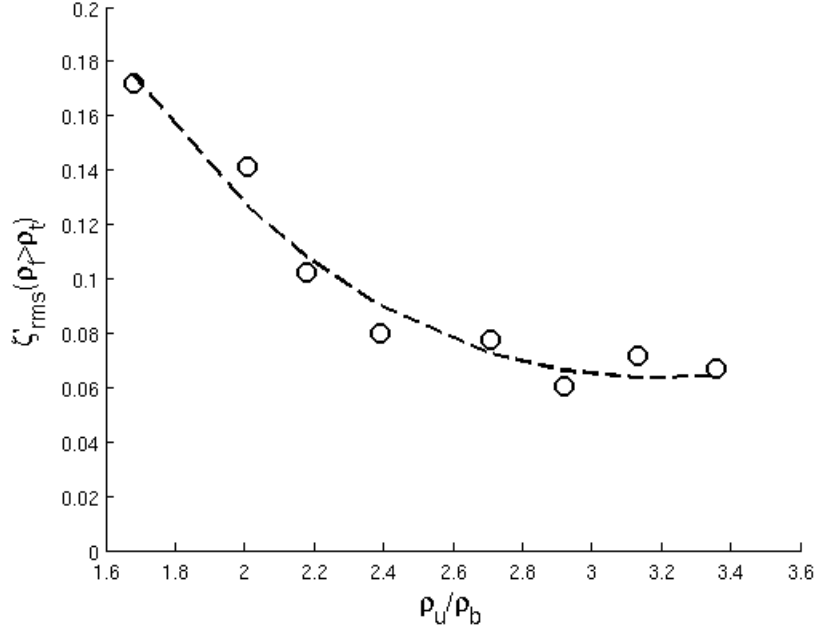


**Figure 23:** Effect of Density Ratio and Intermittency on Limit Cycle Amplitude for the Ballistic Bluff Body at 50 m/s and  $x/D = 3.5$  and  $\rho_t = 0.8$

Finally, averages of the sinusoidal time intervals,  $\tau$  were plotted versus density ratio, with the resulting plot shown in Figure 24.

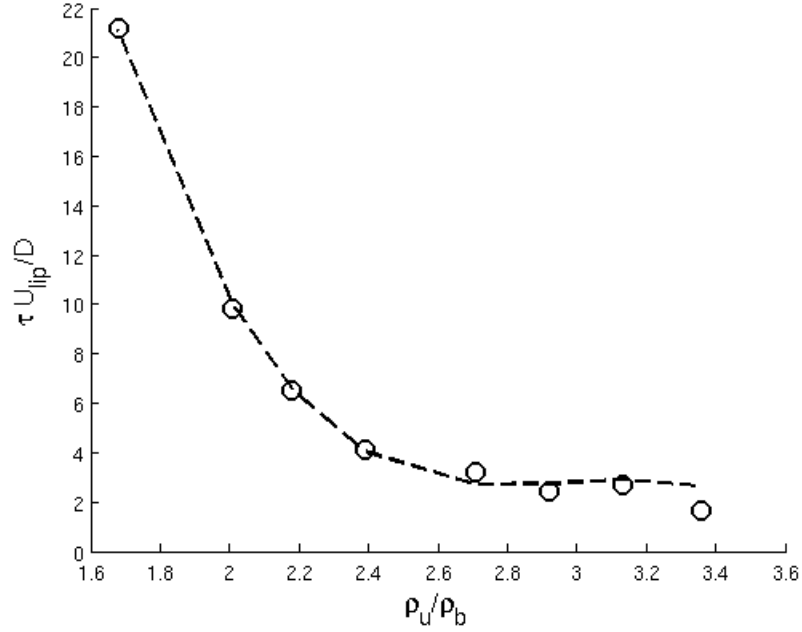


**Figure 24:** Dependence on Density Ratio of the Average Duration of the Times when  $\rho_f > \rho_t$  for the Ballistic Bluff Body at 50 m/s and  $x/D = 3.5$  and  $\rho_t = 0.8$

It can be seen that the sinusoidal bursts monotonically decreases with increasing density ratio.

### 3.3 Comparisons with Parallel Stability Analysis

The experimental results were then compared to the parallel stability analysis described in the Introduction. In order to plot the experimental results on the stability map, as seen in Figure 13, first the backflow and density ratio for each test condition must be calculated. The backflow ratio is defined as

$$\beta = -\frac{u(y=0)}{u(y=\infty)} \quad (10)$$

where  $u$  is axial velocity. In order to calculate the backflow ratio, the axial velocity along the centerline and the freestream velocity obtained from the PIV data were used.

Stability predictions of the normalized temporal growth rate of the absolute instability,  $\omega_{0,i}D/U_{lip}$  were generated and can be seen in Figure 25.

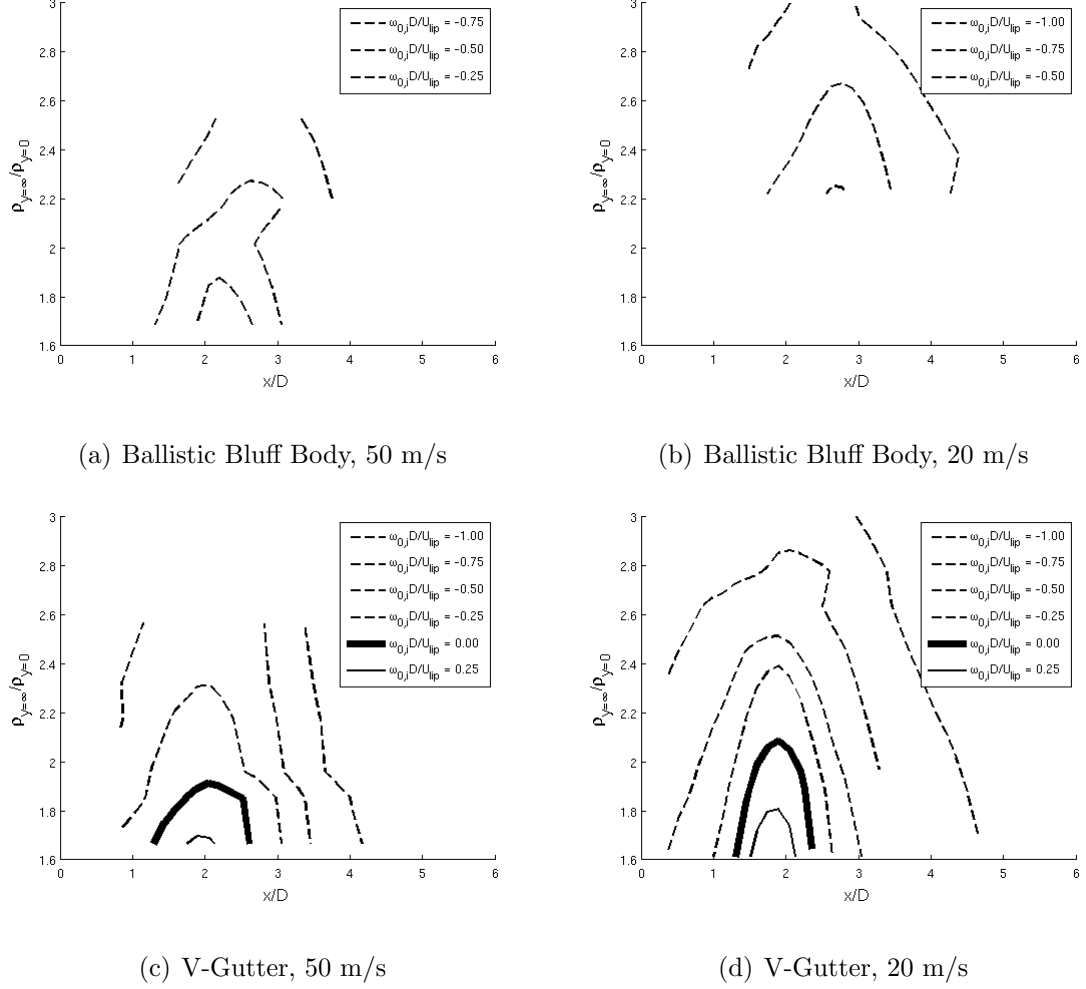


**Figure 25:**  $\omega_{0,1}D/U_{lip}$  Contours vs Axial Position and Density Ratio

Analysis was conducted on data from both the ballistic and v-gutter bluff bodies with lip velocities of 50 m/s and 20 m/s. Absolute instability is indicated by regions of positive absolute instability growth rate and occurs at low density ratios and axial positions of approximately two bluff body diameters downstream. In addition, the absolute instability pocket grows spatially as density ratio decreases. It is important to note that the absolute instability region does not begin immediately after the bluff body. This is due to the low backflow velocities aft of the bluff body.

Next, the measured dependence of centerline velocity fluctuations at  $St_D = 0.24$  on axial location was considered. The resulting profiles were compared to the predicted regions of absolute instability. To compare the two results, the axial coordinate is normalized to the location of maximum absolutely instability growth rate, which directly relates to the location of the maximum reverse velocity. The resulting plot can be seen in Figure 26

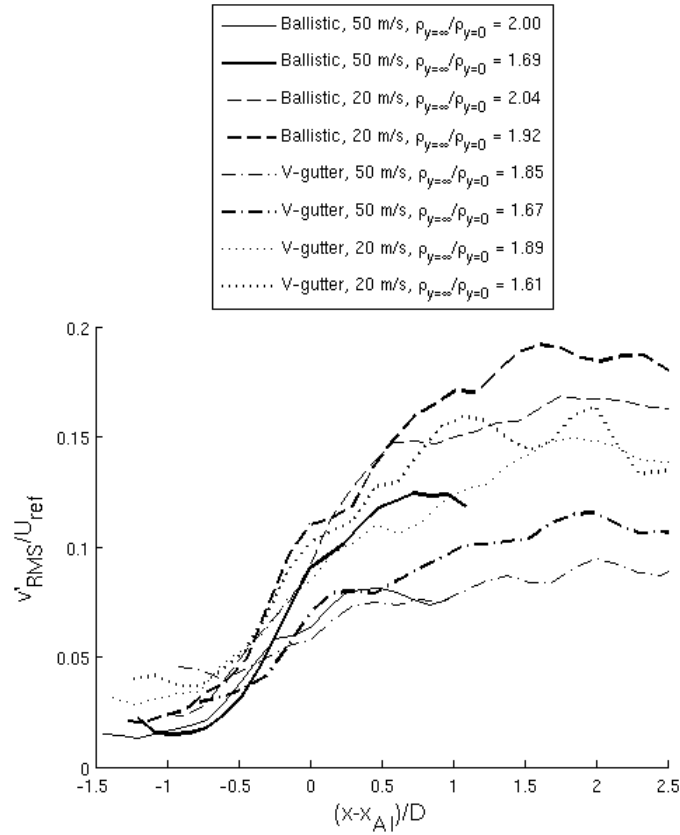


**Figure 26:**  $v'_{RMS}$  vs Downstream Distance from the Predicted Maximum Absolute Instability Growthrate for Ballistic and V-Gutter Bluff Bodies at Multiple Density Ratios and Lip Velocities

Figure 26 shows the narrowband ( $St_D = 0.24$ ) fluctuations beginning to grow at approximately the same referenced location. After the fluctuations have grown in a

region of absolute instability, the structure associated with this mode can continue to amplify as it travels downstream through the convectively unstable region. This is in agreement with the concept that the wake mode, which is characterized by large-scale asymmetric vortex shedding, is initiated by a region of absolute hydrodynamic instability in the wake. Additionally, it should be noted that the location of the region of absolute hydrodynamic instability is predicted by local parallel stability analysis.

Finally, stability characteristics for the ballistic and v-gutter bluff body for the various test conditions were compared. In order to compare the two geometries, the maximum backflow ratio was plotted along with intermittency factor, which is the percentage of time  $\rho_f > \rho_t$  where  $\rho_t = 0.5$ . The resulting plot can be seen in Figure 27.

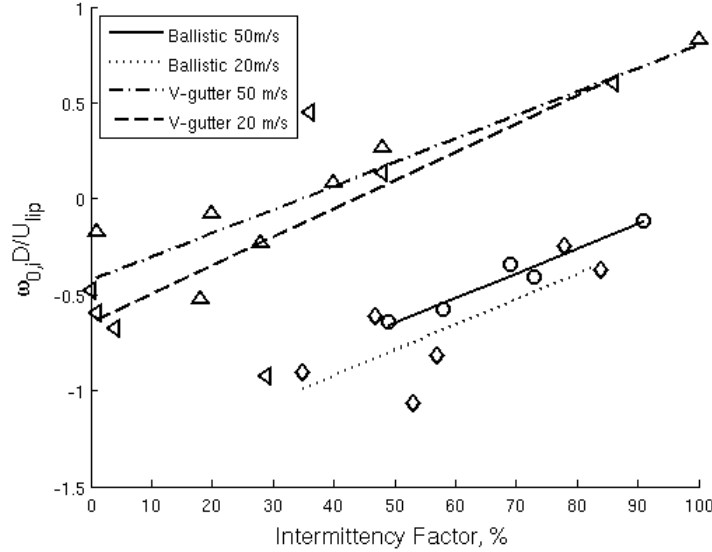


**Figure 27:** Predicted Growth rate vs measured intermittency for both bluff bodies and lip velocity

It can be seen that there is a strong correlation between the intermittency and absolute instability growth. Additionally, it is interesting to note that the slope of the four sets of data are similar and the absolute instability values are consistently lower for the ballistic bluff body than the v-gutter.

## CHAPTER IV

### CONCLUSIONS

- The results clearly illustrate that the dominant instability in the bluff body wake is a strong function of the density ratio, with no sharp bifurcation occurring with variations of the density ratio.
- It was shown that at intermediate density ratios, the two instabilities alternate intermittently, with the BvK instability being dominant for longer durations of time and more frequently as density ratio is decreased and the KH instability being dominant for longer durations of time and more frequently as density ratio is increased.
- Parallel flow stability analysis results were used to correlate a variety of the measured features of the reacting bluff body wake. The results show that if the large-scale sinuous motion is occurring in the wake, it came from a location near the maximum absolute instability growthrate.
- Results show that there is a correlation between the wake mode intermittency and the maximum growthrate of absolute instability in the wake.
- Emphasis is placed on the fact that the transition between the convective and absolute instabilities does not rapidly occur at a specific density ratio for the high Reynolds number flow analyzed, which has particular relevance to high Reynolds number vitiated flows, many of which operate at the intermediate density ratios where there is high intermittency occurring.



## REFERENCES

- [1] B. CASTAING, P. HUERRE, M. R. V. H. S. F. G. J. and VIDAL, P. in *Hydrodynamics and Nonlinear Instabilities* (GODRECHE, C. and MENNEVILLE, P., eds.), pp. 81–152, Cambridge: Cambridge University Press, 1998.
- [2] B. EMERSON, J. LUNDRIGAN, D. N. T. L., “Dependence of the bluff body wake structure on flame temperature ratio,” AIAA Aerospace Sciences Meeting including the New Horizons Forum and Aerospace Exposition, 2011.
- [3] B. EMERSON, J. LUNDRIGAN, J. O. D. N. T. L., “Convective and absolute instabilities in reacting bluff body wakes,” ASME Turbo Expo, 2011.
- [4] DOWLING, A. and STOW, S., “Acoustic analysis of gas turbine combustors,” *Journal of Propulsion and Power*, vol. 19.
- [5] EBRAHIMI, H., “Overview of gas turbine augmentor design, operation, and combustion oscillation,” AIAA/ASME/SAE/ASEE Joint Propulsion Conference, 2006.
- [6] H. MONGIA, T. HELD, G. H. and PANDALAI, R., “Challenges and progress in controlling dynamics in gas turbine combustors,” *Journal of Propulsion and Power*, vol. 19.
- [7] HUERRE, P. and MONKEWITZ, P., “Local and global instabilities in spatially developing flows,” *The Computer Journal*, vol. 22, pp. 473–537, 1990.
- [8] LIEUWEN, T. and MCMANUS, K., “That elusive hum,” *Mechanical Engineering*, 2002.
- [9] LIEUWEN, T. and SHANBHOGUE, S., “Dynamics of bluff body flames near blowoff,” AIAA Aerospace Sciences Meeting, 2007.
- [10] P. MEHTA, M. S., “Combustion heat release effects on the dynamics of bluff body stabilized premixed reacting flows,” 41st Aerospace Sciences Meeting and Exhibit, 2003.
- [11] PRASAD, A. and WILLIAMSON, C., “The instability of the shear layer separating from a bluff body,” *Journal of Fluid Mechanics*, vol. 333, 1997.
- [12] PREETHAM, H. S. and LIEUWEN, T., “Dynamics of laminar premixed flames forced by harmonic velocity disturbances,” *Journal of Propulsion and Power*, vol. 24, 2008.

- [13] R. ERICKSON, M. SOTERIOU, P. M., “The influence of temperature ratio on the dynamics of bluff body stabilized flames,” 44th AIAA Aerospace Sciences Meeting and Exhibit, 2006.
- [14] RANI, S., “Reduced-order model for combustion instability in a two-dimensional duct with a flameholder,” *Journal of Propulsion and Power*, vol. 25, 2009.
- [15] S. BUSH, E. G., “Reacting and nonreacting flowfields of a v-gutter stabilized flame,” *AIAA Journal*, 2007.
- [16] S. DECRUIX, T. SCHULLER, D. D. S. C., “Combustion dynamics and instabilities: Elementary coupling and driving mechanisms,” *Journal of Propulsion and Power*, vol. 19.
- [17] S. KHOSLA, T. LEACH, C. S., “Flame stabilization and role of von karman vortex shedding behind bluff body flameholders,” AIAA/ASME/SAE/ASEE Joint Propulsion Conference, 2007.
- [18] S. SHANBHOGUE, D. P. and LIEUWEN, T., “The k-h instability of reacting, acoustically excited bluff-body shear layers,” AIAA/ASME/SAE/ASEE Joint Propulsion Conference, 2007.
- [19] S. SHANBHOGUE, S. H. and LIEUWEN, T., “Lean blowoff of bluff body stabilized flames: Scaling and dynamics,” *Progress in Energy and Combustion Science*, vol. 35, pp. 98–120, 2008.
- [20] T. LIEUWEN, D. P. and SHIN, D., “Dynamics of a longitudinally forced, bluff body stabilized flame,” AIAA Aerospace Sciences Meeting, 2009.
- [21] T. POINSOT, A. TROUVE, D. V. S. C. and ESPOSITO, E., “Vertex-driven acoustically coupled combustion instabilities,” *Journal of Fluid Mechanics*, vol. 177.